Energy Advances

ROYAL SOCIETY OF CHEMISTRY

PAPER

View Article Online
View Journal

Cite this: DOI: 10.1039/d5ya00380f

An aqueous lithium polyacrylic acid binder enables sulfur distribution and high active material loading to enhance Li–S battery performance

Dharmapura H. K. Murthy, Pranjalee Ghosh, Syeda Reha Khadri and Manu U. M. Patel *

Lithium–sulfur (Li–S) batteries are considered next-generation batteries due to the multiple advantages of using cost-effective sulfur as a cathode material. The development of high-performance and sustainable Li–S battery cathodes demands high active material loading and replacement of traditionally used toxic solvents to dissolve binders in electrode fabrication. Herein, we demonstrate the application of lithium polyacrylic acid (LiPAA) as an aqueous binder to realize high active material loading in Li–S battery cathodes. This approach offers a safe and environmentally friendly alternative that enhances performance compared to the widely employed conventional polyvinylidene fluoride (PVDF) binder, which is processed with the toxic solvent *N*-methyl-2-pyrrolidone (NMP). Optical spectroscopy and microscopy analyses revealed sulfur dissolution in NMP solvent during electrode fabrication, resulting in non-uniform sulfur redistribution within the cathode. This structural inhomogeneity adversely affected electrode integrity and contributed to inadequate electrochemical performance of the battery, particularly under high C-rate conditions. In contrast, electrodes fabricated with the LiPAA binder did not show sulfur dissolution and offered better cyclability. Electrochemical impedance spectroscopy was used to investigate and understand the differences in the battery performance of the prepared electrodes. Our results underscore LiPAA as a viable, scalable, and environmentally friendly binder system for enhancing the performance and stability of Li–S batteries.

Received 26th December 2025,
Accepted 19th February 2026

DOI: 10.1039/d5ya00380f

rsc.li/energy-advances

1. Introduction

Lithium–sulfur (Li–S) batteries have attracted significant attention as potential alternatives to lithium-ion (Li-ion) technology, owing to their high theoretical energy density (2500 Wh kg^{-1}) and specific capacity (1675 mAh g^{-1}), coupled with the low cost and natural abundance of elemental sulfur (S_8).[1–3] Although the Li–S system has several advantages, commercialization has not been possible due to several challenges. For example, S_8 inherently has low electrical conductivity. To address this challenge, additional conductive materials, such as carbon, are mixed with S_8. However, such composites add inactive mass due to carbon loading, thereby reducing the overall energy density of the battery.[4,5] Unlike Li-ion battery cathodes, where solid–solid transitions occur, the Li–S battery cathode undergoes solid (S_8)–liquid ($Li_2S_{n(n=8-2)}$)–solid (Li_2S) transitions. These kinds of transitions occurring during (dis)charging result in a process called polysulfide (PS) shuttling. This process causes capacity decay, anode poisoning, low coulombic efficiency, and active material loss from the cathode, collectively leading to premature battery failure.[6–8] To address these challenges, different types of carbon matrices, electrolytes, electrolyte additives, and modified separators[6,9–12] have been extensively employed over the last decade.

Among the different parameters investigated to enhance the Li–S battery performance, the role of the binder is often ignored and requires careful consideration. Although the total mass of the binder in the cathode is 5–10%, it plays a crucial role in (i) maintaining the structural integrity of active materials during cycling to mitigate volume changes and delamination, (ii) ensuring high electronic conductivity, and (iii) improving the electrolyte wettability to facilitate Li-ion migration in the electrodes. Therefore, the binder is crucial to enhance the stability of the electrodes and improve the overall electrochemical performance.[13–17]

Earlier reports employing polyvinylidene fluoride (PVDF), polymeric ionic liquids (PILs), and saccharide-based binders demonstrated the importance of the binder in the performance of Li–S batteries.[18–20] The general approach in the preparation of Li–S battery cathodes involves the dissolution of the PVDF binder in *N*-methyl-2-pyrrolidone (NMP) and homogenous

Department of Chemistry, Manipal Institute of Technology, Manipal Academy of Higher Education, Manipal, Karnataka, India. E-mail: Manu.patel@manipal.edu

dispersion of a carbon/S_8 composite in the same solvent to form a slurry. The formed slurry is further coated onto an aluminium current collector followed by drying to obtain the required electrodes. Apart from the toxicity concern of NMP, PVDF as a binder is associated with various other challenges. Cathode electrodes with PVDF binders are known to delaminate due to volume expansion taking place in the electrode during cycling, resulting in battery failure.[19–23] Efforts have been made to identify alternative binders to overcome the challenges associated with PVDF and NMP systems.[18–20] For Li–S batteries to be commercially viable as high-energy-density systems, they must deliver areal capacities of at least 4 mAh cm^{-2}.[24,25] However, many reported studies fall short of this requirement, often due to limitations associated with the binder system. PVDF, when used with carbon/S_8 composites, exhibits weak interfacial adhesion, high electrical resistance, and poor tolerance to the large volume changes occurring in the cathode during cycling.[22,26,27] The earliest report on the use of polyacrylic acid (PAA) as an alternative to PVDF binders in Li–S batteries appeared in 2012. In this foundational study, Zhang *et al.* systematically compared PVDF and PAA binders, revealing distinct advantages of PAA over PVDF for electrode stability and electrochemical performance.[28]

Here, we examine lithium polyacrylic acid (LiPAA) as a promising alternative binder for high-S_8-loading cathodes in Li–S batteries, emphasizing its ability to sustain electrode integrity and accommodate high active material loading while delivering superior electrochemical performance. To understand the mechanisms underlying the observed performance differences, UV-visible spectroscopy and scanning electron microscopy (SEM) were employed to examine S_8 dissolution and redistribution. Electrochemical impedance spectroscopy (EIS) was used to probe variations in electrode structure. Together, these analyses reveal that LiPAA enhances battery stability, rate capability, and active material utilization compared to conventional and extensively studied PVDF-based cathodes.

2. Experimental

2.1. Materials

Vulcan carbon (XC-72, Tanaka Kikinzoku Kogyo), sodium thiosulfate ($Na_2S_2O_3{\cdot}5H_2O$, 99.5%, Sigma-Aldrich), HNO_3 (Sigma-Aldrich), polyacrylic acid (PAA, MW $\approx$ 250 000; Sigma-Aldrich), NMP (Sigma-Aldrich), distilled water, LiOH (Sigma-Aldrich), PVDF (Kynar HSV900), bis(trifluoromethanesulfonyl)imide lithium (LiTFSI, battery grade, Sigma-Aldrich), lithium nitrate ($LiNO_3$, Sigma-Aldrich), 1,3-dioxolane (DOL, anhydrous, Sigma-Aldrich), tetrabutylammonium bis-trifluoromethanesulfonimidate (TBATFSI, Merck), 1,2-dimethoxyethane (DME, anhydrous, Sigma-Aldrich), and metallic lithium (Sigma-Aldrich) were used in this study.

2.2. Methods

2.2.1. Preparation of the carbon–sulfur (C/S_8) composite. The C/S_8 composite was obtained by the wet impregnation method.[29] 1.5 g of vulcan carbon was first dispersed in 120 mL of $Na_2S_2O_3{\cdot}5H_2O$ using ultrasonic treatment for 20 minutes under continuous stirring. Once a well-dispersed suspension was formed, 250 mL of 1 M HNO_3 was slowly added to the homogenous carbon suspension. Following the addition of HNO_3, the suspension was continuously stirred for 20 min under ultrasonic treatment. After 20 min, the suspension was allowed to settle, and the supernatant was decanted. The settled C/S_8 composite suspension was washed with distilled water until a neutral pH was reached and filtered to obtain the C/S_8 composite. The C/S_8 composite was dried for 72 h at 80 °C in a vacuum drier. Thermogravimetric analysis (TGA) revealed that the prepared C/S_8 composite contained an S_8 loading of 68%.

2.2.2. Synthesis of the LiPAA binder and preparation of PVDF solution. A known amount of PVDF powder was dissolved in a known volume of NMP by stirring overnight to obtain a 10% PVDF solution. Aqueous LiPAA binder was synthesized by an ion exchange process using PAA and LiOH. A weighed amount of PAA was dissolved in distilled water under continuous stirring overnight, yielding a 25% (w/v) solution. An equimolar amount of LiOH dissolved in distilled water was added to the PPA solution until the solution pH was neutral, leading to the formation of the LiPAA binder. Thus, the prepared solution contained 3% LiPAA binder.

2.2.3. Preparation of cathodes with LiPAA and PVDF binders. Electrodes with the PVDF binder were prepared by dispersing the C/S_8 composite into a suspension of 10% PVDF in NMP. The mixture was formulated to yield a slurry composition of 90 wt% C/S_8 composite and 10 wt% PVDF. For LiPAA electrodes, the C/S_8 composite was dispersed into a suspension of 3% LiPAA in water. The mixture was composed of 90 wt% C/S_8 composite and 10 wt% LiPAA. No additional carbon black was used in either of the slurries. The slurries were homogenized by vigorous mixing for 1 h and then cast onto aluminum foil (16 μm thick) with a Mayer rod set to a wet-film thickness of 400 μm. In this study, bare aluminum foil was employed as the current collector rather than carbon-coated aluminum foil to enable a direct and unbiased evaluation of binder performance. This approach isolates the intrinsic effects of binder chemistry by eliminating additional contributions arising from surface modification or conductive carbon coatings on the substrate. The electrodes were dried at room temperature for 72 h. Circular electrodes were then punched out and dried further at 80 °C for 12 h before battery assembly. The resulting cathodes had an S_8 loading of 2.5 $\pm$ 0.1 mg cm^{-2}, translating to 4.0 mAh cm^{-2} capacity. Uncalendared electrodes were used in the coin cells for battery performance evaluation and the first set of EIS measurements.

2.2.4. Preparation of standard samples and UV-visible analysis of binder solvents. A known amount of S_8 was added to NMP and distilled water and stirred for 24 h to obtain a 1 mM S_8 solution in each solvent. Binder solutions of LiPAA and PVDF, along with their solvents (distilled water and NMP), were used directly for UV-visible spectroscopy. Distilled water and NMP were also extracted from C/S_8 composite slurries. The slurry composition stayed the same; only the solvent extraction

time was varied. S_8 is not expected to dissolve in water, so slurries were left for 24 h before extracting the solvent. For NMP, the solvent was extracted after 30 min to represent the minimum processing time for electrode preparation. The extracted solvents were then used for UV-visible measurements.

2.2.5. Coin cell battery assembly and electrochemical measurements. The electrolyte was prepared by dissolving 1 M LiTFSI and 0.25 M $LiNO_3$ in a 1 : 1 (v/v) mixture of DOL and DME. $LiNO_3$ was used to promote SEI formation on the lithium anode, thereby extending battery life. Coin cells (CR2032) were assembled with a 15 mm cathode, a 15 mm lithium anode, and an 18 mm Celgard H2013 separator. To ensure adequate electrolyte uptake for optimal battery performance, three layers of separators were inserted between the electrodes. The cells were filled with 80 μL of electrolyte consisting of 1 M LiTFSI and 0.25 M $LiNO_3$ dissolved in DOL : DME, equivalent to 32 μL per milligram of S_8 in the cathode. The assembled batteries were cycled with a Metrohm Autolab battery tester. For EIS measurements, symmetrical cells with cathodes were assembled. Two 15 mm cathodes were used along with three layers of Celgard separators, and 80 μL of 100 mM TBATFSI in DOL : DME was used as the electrolyte. For battery performance testing, we used 1 M LiTFSI and $LiNO_3$ in DOL : DME electrolyte as this electrolyte enables realistic electrochemical performance evaluation, including cycling stability.[6] TBATFSI was not used in cells for battery cycling considering the large size of TBA^+ cations compared to Li^+ ions that facilitate faster ionic conductivity at higher C-rate cycling. Therefore, the performance claims in the manuscript are based exclusively on LiTFSI and $LiNO_3$ in the DOL : DME electrolyte system.

3. Results and discussion

Fig. 1 compares the UV-visible spectra between PVDF in NMP and LiPAA in distilled water along with the supernatant obtained from their respective composite inks. Fig. 1a shows the UV-visible spectrum of the supernatant of the ink with the PVDF binder. The obtained spectrum confirmed the dissolution of S_8 in NMP during the ink preparation. The absorption peak at 280 nm indicates the dissolution of S_8, as the obtained peak matched the standard S_8 in NMP solution.[30] Within 30 min, approximately 3 mM of S_8 was dissolved in NMP, corresponding to ~16% of the total S_8 in the ink. This dissolution process ultimately facilitates the redistribution of S_8 within the electrode, leading to the undesired outcomes discussed later in the study. Fig. 1b shows the UV-visible spectrum of the standard S_8 in water. It can be seen from the spectrum that negligible or no solubility was observed, with no detectable dissolution even after 24 h of continuous stirring. The UV-visible spectrum of the supernatant of the prepared ink formulated with the LiPAA binder showed no characteristic S_8 absorption features, indicating the absence of dissolved S_8 species in the system. However, an absorbance peak at 260 nm was detected, which corresponds to the LiPAA binder dissolved in water. This peak matches the characteristic spectrum of LiPAA in aqueous solution. The key takeaway from the UV-visible results is that S_8 dissolves from the composite when NMP is used during electrode fabrication. This dissolution may cause S_8 to redistribute unevenly within the electrode.

Fig. 2 shows the SEM micrographs of the fabricated electrodes with PVDF and LiPAA binders, taken from the top and in the cross-section. Fig. 2a and b present the surface and cross-sectional views of the PVDF-based cathode, respectively. Both reveal a distinct S_8 layer on the surface and within the electrode. Fig. 2c and d display the surface and cross-sectional SEM micrographs of the electrode with the LiPAA binder, which clearly lack the S_8 layer and show a homogeneous distribution of components. Further SEM images show open pores and an even distribution of materials in the electrode. Overall, the LiPAA-based cathode avoids S_8 dissolution during processing, as confirmed by UV-visible spectroscopy (Fig. 1b), and achieves a homogeneous distribution of electrode components. Additional evidence for S_8 redistribution in PVDF-based electrodes is provided by XRD and EDX analyses (Fig. S1 and S2). XRD patterns obtained from PVDF and LiPAA-based electrodes both show the characteristic diffraction peaks of crystalline S_8 (JCPDS no. 08-0247); however, the PVDF electrode (Fig. S1a)

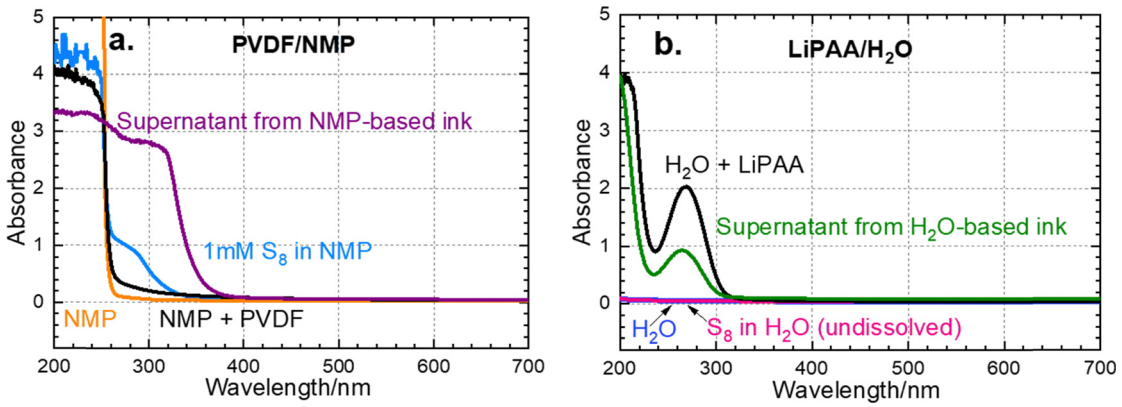

Fig. 1 (a) UV-visible spectra of NMP, NMP + PVDF, 1 mM standard S_8 in NMP, and the supernatant extracted from PVDF electrode slurry. (b) UV-visible spectra of H_2O, LiPAA + H_2O, 1 mM standard S_8 in H_2O, and the supernatant extracted from LiPAA electrode slurry.

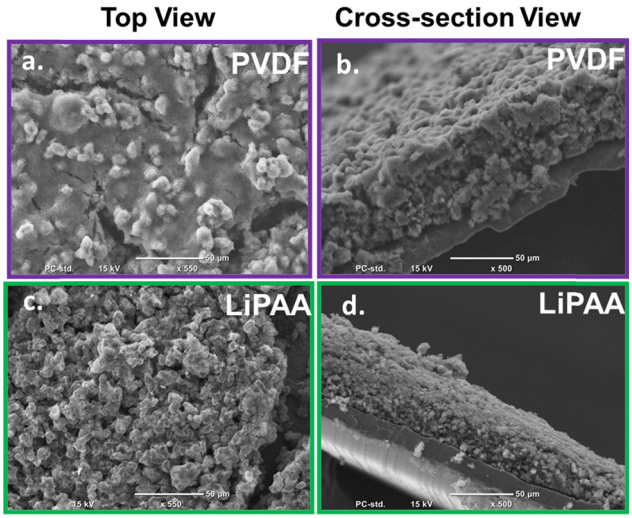

Fig. 2 (a) PVDF-based cathode showing clogged pores and cracks. (b) PVDF-based cathode showing an S_8 layer deposited on the carbon black across the electrode. (c) LiPAA-based cathode showing open pores. (d) LiPAA-based cathode showing a homogenous distribution of electrode components.

exhibits higher peak intensities, indicating greater S_8 accumulation on the electrode surface. Consistently, EDX analysis reveals a higher surface S_8 content in PVDF-based electrodes (20%) compared to LiPAA-based electrodes (14%) (Fig. S2a and b). Together, these results confirm enhanced S_8 redistribution and surface deposition in the PVDF system. These observations confirm the dissolution and subsequent redistribution of S_8 in NMP, consistent with the UV-visible spectroscopy results presented in Fig. 1a. During electrode fabrication, S_8 dissolves in NMP from the carbon pores, enters the liquid phase, and gradually deposits on the electrode surface during drying. This dissolution and recrystallization of S_8 causes uneven active material distribution in the cathode.

To further understand the consequences of S_8 dissolution, redistribution and the influence of binders on battery performance, coin cells were assembled and cycled. Fig. 3 shows the long-term battery cycling capacity and coulombic efficiency of batteries with PVDF and LiPAA binder cathodes. The results discussed here are averages from two batteries per binder-type cathode, all cycled under the same conditions. Cathodes with similar active material loading were carefully selected to avoid discrepancies in battery capacity. The batteries were cycled at C/20 in the initial cycle, followed by long-term cycling at C/5. Initial capacities at C/20 from the PVDF and LiPAA batteries were 1100 mAh g^{-1} and 1050 mAh g^{-1}, respectively, as shown in Fig. 3b. Despite this initial capacity difference, the long-term cycling profiles of both systems coincided. During extended C/5 cycling, the capacity gradually stabilized within the range of 550–600 mAh g^{-1} (Fig. 3b). This stabilization suggests that, after initial structural and interfacial rearrangements, both binder systems can support relatively stable electrochemical performance at low C-rates. A more detailed examination of capacity retention after prolonged cycling revealed clear

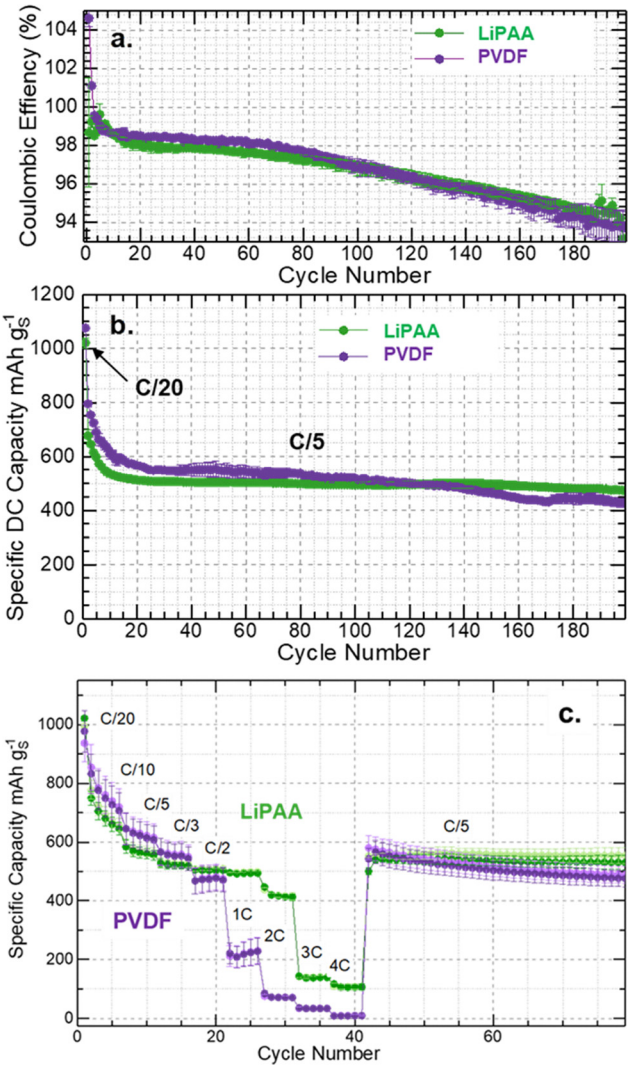

Fig. 3 (a) Obtained coulombic efficiency during long-term cycling of batteries with PVDF and LiPAA cathodes. (b) Obtained specific discharge capacity. (c) Specific capacity obtained from batteries in rate capability tests.

differences between the two binder systems. After 100 cycles at C/5, batteries with the PVDF binder retained 68% of their initial capacity. In contrast, LiPAA-based batteries retained 78% of their initial capacity. The higher capacity retention with LiPAA shows its superior ability to preserve electrode integrity, maintain active-material connectivity, and reduce degradation over time compared to PVDF. After 120 cycles, the PVDF-based cathode showed a much faster drop in capacity than the LiPAA cathode, further confirming the accelerated performance deterioration observed in the PVDF system (Fig. 3b). Earlier research highlights the importance of a uniform distribution of S_8 within the electrode. A uniform distribution of electrode components, including carbon, S_8, and the binder, helps optimize S_8 utilization, enhances ionic and electronic conductivity, and accommodates volume expansion. As a result, the battery can deliver higher energy density and capacity. In contrast, non-uniform S_8 distribution often leads to rapid capacity decay and accelerated electrode degradation.[31,32]

Despite the relatively stable coulombic efficiency observed in the initial cycles, notable differences emerged beyond 90 cycles, where a gradual drop in efficiency was detected in both systems (Fig. 3a). This decline in the coulombic efficiency is indicative of intensified PS shuttling, where soluble lithium PS migrate between the cathode and anode. Shuttling reactions lead to irreversible capacity loss and reduced cycle stability by consuming the active material. The onset of significant PS shuttling after extended cycling underscores the challenges associated with high-S_8-loading cathodes, where larger quantities of soluble PS intermediates are generated, requiring effective confinement strategies to maintain cycling efficiency. However, the reduced capacity in this study can be attributed to the high S_8 loading in the cathode and the absence of specialized or modified carbon black used in the composite.[33,34] Further differences between the two binder systems became evident after approximately 100 cycles, where the cycling stability and coulombic efficiency of the PVDF batteries began to deteriorate rapidly, as shown in Fig. 3a. The loss of stability in the PVDF system is likely associated with its weaker interaction with the C/S_8 composite, dissolution intermediates, and volume changes, which compromise the electrode integrity during prolonged cycling. In contrast, the LiPAA-based electrodes demonstrated comparatively better performance, as evidenced by their better capacity retention and more stable cycling response, even though they were subjected to the same electrode formulation constraints (Fig. 3b). This difference highlights the beneficial role of the LiPAA binder in providing stronger interactions with the active materials and better mechanical stability under repeated cycling stress.

Further evidence for the above discussion on the difference in the performance of the batteries can be found in the rate-capability measurements of both binder systems, as shown in Fig. 3c. The batteries were cycled at different C-rates and analyzed for their electrochemical performance. At higher C-rates, electrochemical evaluation revealed distinct differences between cells fabricated with LiPAA and PVDF binders. During the initial low-rate cycling, both binder systems exhibited comparable behaviors (Fig. 3c). However, LiPAA-based electrodes exhibited markedly improved capacity retention and cycling stability at higher current densities (1C to 4C). Batteries with the PVDF binder cathode delivered capacities of approximately 200, 90, 40, and 10 mAh g^{-1} at 1C, 2C, 3C, and 4C, respectively. In contrast, LiPAA binder-based cathode batteries delivered capacities of 500, 410, 140, and 100 mAh g^{-1} at the same C-rates, as shown in Fig. 3c. The capacities obtained from LiPAA-based batteries were significantly superior to those obtained from PVDF binder-based batteries. Furthermore, when the batteries were switched to low C-rate (C/5) cycling, differences in the delivered capacity were observed between the two binder systems. The capacity of PVDF batteries deteriorates with cycling, whereas LiPAA binders enable stable cycling, as shown in Fig. 3c. Based on earlier findings, capacity degradation in Li–S batteries following C-rate measurements is primarily associated with the PS shuttle phenomenon and electrode degradation due to volume expansion. The cathode experiences the buildup of insulating Li_2S layers, along with the loss of interparticle contacts and delamination. This combination restricts electron and ion transport, limits further redox reactions, and increases the internal resistance in the cell. In the presence of the PVDF binder, these degradation pathways accelerate under high C-rate operation.[35–37] S_8 dissolution and the generation of supersaturated intermediates promote excessive precipitation of Li_2S, which electrochemically depletes the active material. Electrode structural integrity degradation may also contribute to the decline in battery capacity. The stability of LiPAA batteries can be attributed to the stronger interactions between LiPAA and the carbon matrix. These interactions support the electrode integrity by accommodating volume changes and mitigate active material loss during repeated cycling. In contrast to PVDF, LiPAA-based cathode batteries maintained a consistent performance, highlighting their robustness at higher C-rates. Based on the delivered specific capacity of 500 mAh g^{-1} from LiPAA-based electrodes at C/5, the corresponding partial energy density at the pouch-cell level is estimated to be approximately 420 Wh kg^{-1}. Postmortem analysis of the electrodes recovered from the cells can provide more information on the degradation phenomenon. Efforts were made to recover electrodes from the cycled batteries for postmortem analysis; however, recovering intact and representative cathodes after cycling for a prolonged period proved challenging due to the substantial volume changes associated with S_8 conversion reactions. Effects often led to partial delamination or structural collapse upon disassembly, making it difficult to obtain reliable and artefact-free SEM images for meaningful comparison.

EIS was used to further understand the difference in battery performance between PVDF and LiPAA binder electrodes. Symmetrical coin cells with PVDF and LiPAA binders were assembled with a non-intercalating TBATFSI electrolyte. In the full cell configuration, multiple elementary processes occurring at each of the electrodes make it difficult to deconvolute the obtained results.[28] Symmetrical cell configuration is considered due to its multiple advantages in elucidating the obtained impedance spectra.[38–40] To describe the ionic transport behavior within the electrolyte-filled pores of the conductive electrode network, the transmission line model (TLM) was considered. This equivalent circuit framework, commonly used for interpreting EIS data of Li-ion battery electrodes, provides a realistic representation of distributed ionic and electronic pathways. Previous studies have shown that the electronic resistance in a well-designed Li-ion battery is very small due to the presence of conductive carbon in the electrodes.[41–43]

Given its negligible contribution to total resistance, electronic resistance is usually not considered. However, the ionic resistance is significantly high owing to solid-to-liquid phase charge-transfer reactions.[44] To mitigate the higher ionic resistance, blocking conditions can be considered using non-intercalating electrolyte salts such as TBATFSI. This approach enabled the generation of simplified yet reliable results, facilitating clearer comparison between cathodes prepared using PVDF and LiPAA binders. EIS spectra were measured between 100 kHz and 100 mHz at 25 °C. The obtained resistance responses were divided by two, as it is the total contribution

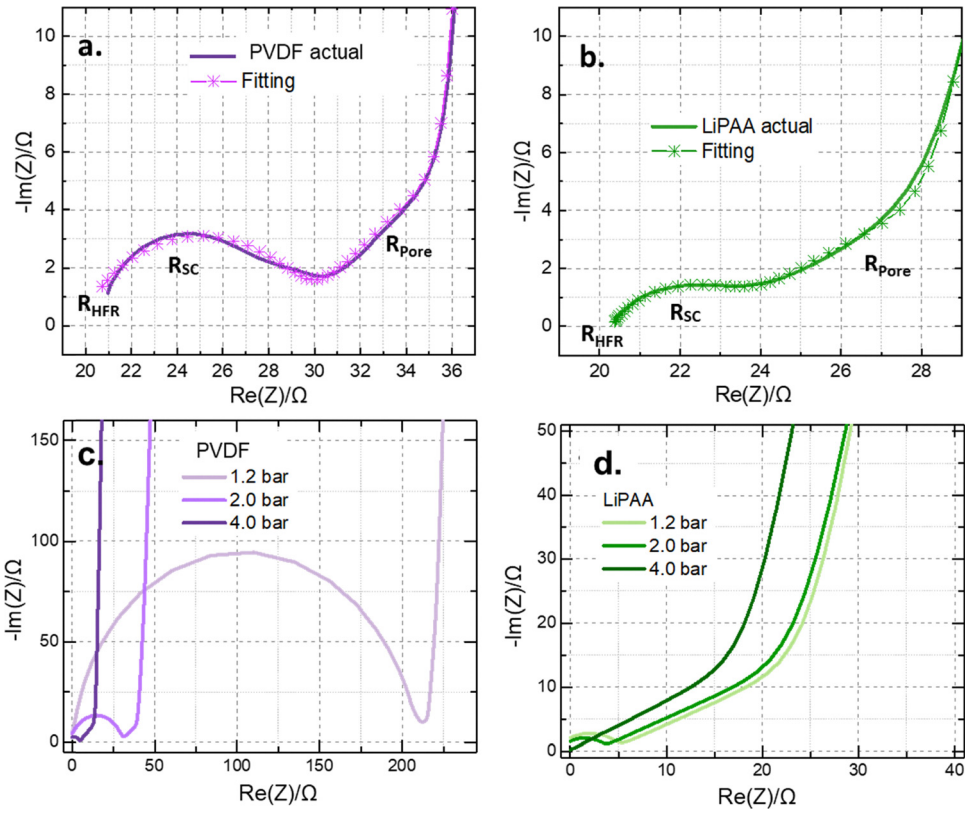

Fig. 4 EIS from symmetrical cells: (a) and (b) spectra and fitting of PVDF and LiPAA-based electrodes; (c) and (d) spectra of PVDF and LiPAA-based electrodes compressed at different pressures.

of two identical electrodes. Fig. 4a shows the EIS data obtained with PVDF cathode cells, and Fig. 4b shows the EIS data obtained with LiPAA cathode cells. The TLM under blocking conditions provides an excellent fit to the data, as indicated by the asterisks and line combination for both PVDF and LiPAA, presented in Fig. 4a and b. The expected EIS data under the mentioned working conditions and the observed spectra, along with the proposed electric circuits, are shown in Fig. S3a and b (SI). The expected EIS data should have a 45 degree slope at high frequencies and a vertical line at low frequencies, which corresponds to the resistance from the separator and finite space Warburg element that corresponds to the mass transport (ion diffusion) within the electrodes (as shown in Fig. S3a).[41–43] However, we obtained a semicircle at high frequency (100 kHz) followed by the expected 45 degree slope and subsequent vertical line in the case of both PVDF and LiPAA-based binder electrodes (Fig. 4a and b). As discussed earlier, electronic resistance is negligible, and the ionic resistance was eliminated by employing a non-intercalating electrolyte; therefore, the observed semicircle must arise from another resistance element within the electrode.

A closer comparison of the EIS data from the PVDF and LiPAA-based cathodes reveals that the measured resistance primarily arises from three contributions: the high-frequency resistance associated with the separator (R_{HFR}), an additional resistance component responsible for the semicircle (R_{SC}), and the pore resistance within the cathodes (R_{Pore}) at low frequency. The values corresponding to these contributions are listed in Table 1. Table 1 shows that the high-frequency resistance is comparable for both electrodes (PVDF and LiPAA), as it arises from the separator. However, the PVDF-based electrode exhibited a 13% higher pore resistance than the LiPAA-based electrode. This increase is likely due to the deposition of the S_8 layer on the surface, which clogs the electrode pores, as confirmed by the SEM micrographs (Fig. 2a and b). Additionally, the additional resistance component R_{SC} substantially contributes to

Table 1 The three factors contributing to the observed resistances in the PVDF and LiPAA cathodes

Resistance (R)	PVDF R in Ω	LiPAA R in Ω	Difference in R
R_{HFR}	10.10 ± 0.45	10.15 ± 0.52	No significant difference
R_{SC}	5.73 ± 1.05	1.33 ± 0.14	PVDF electrodes show a 330% higher resistance
R_{Pore}	8.5 ± 0.51	7.5 ± 0.25	PVDF electrodes show a 13% higher resistance

The total observed resistance is the sum of $R_{HFR} + R_{SC} + R_{Pore}$. Resistance values from each factor are extracted from the EIS data and divided by two, as we are using symmetric cells.

the overall resistance of the PVDF cathode. The calculated R_{SC} value for the PVDF cathode was 330% higher than that for LiPAA, suggesting that this element (R_{SC}) plays a dominant role in limiting the battery performance under higher C-rate cycling. Comprehensive studies by Landesfeind *et al.* and Gaberšček *et al.* revealed that the high-frequency semicircles (R_{SC}) commonly observed in the EIS of Li-ion battery electrodes originate primarily from contact resistance at the electrode–current collector interface.[45–47] From their studies, it was apparent that the high-frequency impedance semicircle (R_{SC}) primarily highlights the contact resistance between the electrode composite and the metallic substrate, such as aluminum, along with the double-layer capacitance that forms on the substrate when it comes into contact with the electrolyte.[45–47] Fig. S3b presents the proposed equivalent circuit for the EIS data with the semicircle, where an additional parallel resistor–capacitor element is incorporated into the baseline circuit shown in Fig. S3a.

To further confirm that the origin of the high-frequency impedance semicircle is due to the contact resistance in the electrodes, we performed EIS of the compressed PVDF and LiPAA electrodes. Fig. 4c and d show the EIS spectra of the electrodes coated on aluminum current collectors and compressed at 1.2, 2.0, and 4.0 bar. The spectra were shifted to the origin of the complex plane for easier comparison. At medium and low frequencies, all samples displayed the expected TLM behavior. However, differences appeared at high frequencies. The PVDF-based electrode compressed at 1.2 bar shows a clear semicircle, with a resistance of ~100 Ω. In the case of electrodes compressed at 2.0 bar, the semicircle remains, but the resistance decreases to ~16 Ω, and in the electrodes compressed at 4.0 bar, the semicircle nearly disappears, as shown in Fig. 4c. A similar trend was observed for the EIS results of the LiPAA-based electrodes. However, the initial resistance was ~2.5 Ω, and the decrease in resistance was minimal when the compression pressure increased from 1.2 to 2.0 bar. At 4.0 bar, the semicircle completely disappears in the EIS (Fig. 4d). This trend suggests that the semicircle originates from the electronic resistance, which is reduced by higher compression. The contact resistance may arise from either the interparticle resistances in the electrode or the contact resistance at the current collector–electrode interface. Since S_8 was dissolved and redistributed within the electrode, the observed resistance was likely a combination of the interparticle resistance and the contact resistance at the aluminum/electrode interface. These results align with those of Landesfeind *et al.* and Gaberšček *et al.*, who also linked the high-frequency semicircle to the current collector/contact resistance and observed its reduction with pressure.[45–47]

Earlier studies have demonstrated that variations in temperature can significantly influence the impedance behaviour of Li–S electrochemical cells.[48] To understand the influence of temperature on the EIS results of the PVDF and LiPAA electrodes, we measured the EIS spectra at 10 °C and 45 °C. No significant difference or impact of temperature on the electrodes was observed (Fig. S4), further suggesting that the R_{SC} element is due to interparticle resistance and contact resistance in the electrodes.

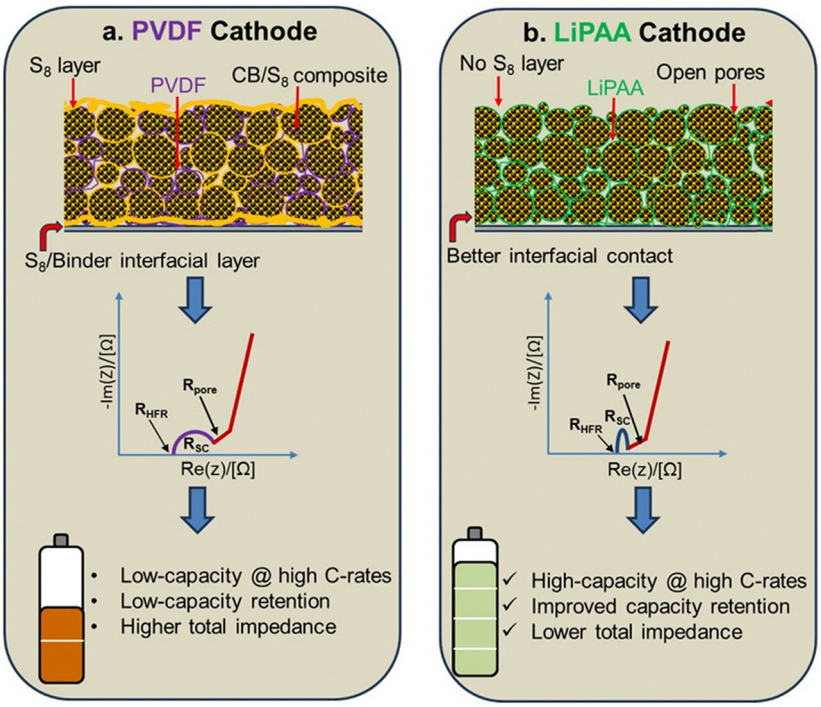

Fig. 5 The proposed model of Li–S cathode behavior with (a) the PVDF binder cathode and (b) the LiPAA cathode and their respective influence on EIS and battery performance.

Schematic representations of the cross-sections of the CB/S_8 composite, PVDF, and LiPAA binder electrodes are shown in Fig. 5. Fig. 5a shows the cross-section of the PVDF electrode. The elemental S_8 encapsulated in the pores of the carbon black dissolves in NMP and gets redistributed across the electrode. The redistribution of elemental S_8 occurs not only on the surface of the cathode but also at the interface of the carbon composite and aluminum current collector and between the carbon black particles in the electrode. Once the electrodes are dried, the dissolved S_8 recrystallizes, leading to the formation of a non-conductive layer between the carbon particles, carbon composite, and aluminum current collector, which increases the total contact resistance in the electrode, as observed in the EIS measurements (Fig. 4a). The impact of this increased contact resistance is clearly visible in the battery performance at higher C-rates, as shown in Fig. 3c. The possible reasons for the inferior battery performance can be linked to the deposition of Li_2S particles (discharge product) on the surface of the carbon black and the carbon composite–current collector interface along with delamination and loss of interparticle contact. As Li_2S is a highly insulating material, it further facilitates the deterioration of battery performance owing to reduced contact. When the PVDF-based electrodes were compressed at different pressures, the S_8 layer present between the carbon black particles and at the current collector interface was disrupted, thereby reducing the overall contact resistance, as shown in Fig. 4c. In comparison, the distribution of the CB/S_8 composite in the electrode with the LiPAA-based binder was significantly different.

As confirmed by UV-visible spectroscopy and SEM, S_8 dissolution did not occur in water, and as a result, the encapsulated S_8 was retained inside carbon black. This led to a more homogeneous distribution of all electrode components, as shown in Fig. 5b. Because there is no S_8 layer between the carbon particles and the current collector interface, the overall contact resistance is significantly low, as observed by EIS (Fig. 4b). Although we observe minimal contact resistance, this could arise from the small space between the carbon composite particles and current collectors. Collectively, these findings indicate that LiPAA binders provide distinct advantages over PVDF in maintaining long-term electrochemical stability under demanding operating conditions, highlighting their suitability for high-active-material-loading and high-C-rate Li–S cathodes. Commonly used water-based binders, such as CMC–SBR systems, offer good mechanical flexibility and adhesion; however, they often present processability challenges like high slurry viscosity, sensitivity to solid loading, and the need for careful control of pH and mixing order to ensure uniform dispersion.[49,50] In contrast, LiPAA offers simpler slurry processing and good rheological control, making it more suitable for scalable cathode electrode manufacturing. Furthermore, quasi-solid-state Li–S batteries typically exhibit higher interfacial and charge-transfer resistances due to limited electrolyte mobility and restricted electrode–electrolyte contact.[51,52] Addressing these limitations requires binder systems that can facilitate efficient ion transport and maintain intimate interfacial contact. In this regard, the use of LiPAA offers distinct advantages. In the present study, LiPAA markedly reduces interfacial resistance compared to PVDF, which is expected to improve ionic transport across solid or gel-like interfaces. Additionally, LiPAA promotes closer contact among S_8, conductive carbon, and the electrolyte phase. Consequently, LiPAA binders can effectively mitigate resistive losses in quasi-solid-state Li–S systems, thereby supporting enhanced reaction kinetics and improved cycling stability.

4. Conclusions

This study showed the effective use of a water-soluble LiPAA binder for high-active-material-loading Li–S cathodes, presenting a viable alternative to the commonly used NMP-soluble PVDF binder. Due to its processability in water, LiPAA promotes environmentally friendly electrode preparation by eliminating the need for toxic solvents such as NMP. In contrast to the advantages of LiPAA-based electrodes, PVDF-based electrodes processed with NMP suffered S_8 dissolution (as verified by UV-visible spectroscopy, XRD, and SEM), which led to S_8 redistribution and poorer electrochemical performance at high C-rates. Compared to PVDF-based electrodes, those with LiPAA demonstrated superior battery performance, especially at higher C-rates. EIS revealed that lower contact resistance in the LiPAA electrode contributed to its improved battery performance relative to PVDF electrodes. Notably, LiPAA enabled stable cycling at high active material loadings even without optimization of the carbon black in the composite. These results highlight the strong potential for further performance enhancement through the integration of LiPAA with advanced carbon architectures. These findings underscore the potential of LiPAA as a sustainable binder for high-performance Li–S batteries.

Author contributions

Pranjalee Ghosh and Syeda Reha Khadri carried out the synthesis of the carbon/sulfur composite, structural/morphology analyses and electrode fabrication. Dharmapura H. K. Murthy conducted electrochemical and optical spectroscopy analyses and assisted Manu U. M. Patel in writing the manuscript. Manu U. M. Patel wrote the first version of the manuscript, in charge of overall direction, execution of research work, and planning of the manuscript.

Conflicts of interest

The authors declare that they have no known competing financial interests or personal relationships that could have appeared to influence the work reported in this paper.

Data availability

Most of the data generated and analyzed in this study are presented in this article. Additional datasets and scripts

supporting the findings are available from the corresponding author upon reasonable request.

Supplementary information (SI) includes XRD, EDX, expected Nyquist plots, respective electrical circuits, and temperature-dependent EIS results. See DOI: https://doi.org/10.1039/d5ya00380f.

Acknowledgements

M. U. M. Patel thanks Manipal Academy of Higher Education (MAHE) for providing the seed grant (no. 00001567).

References

1 A. Manthiram, Y. Fu and Y.-S. Su, *Acc. Chem. Res.*, 2013, **46**, 1125–1134, DOI: 10.1021/ar300179v.
2 P. G. Bruce, L. J. Hardwick and K. M. Abraham, *MRS Bull.*, 2011, **36**, 506–512, DOI: 10.1557/mrs.2011.157.
3 S. Evers and L. F. Nazar, *Acc. Chem. Res.*, 2013, **46**, 1135–1143, DOI: 10.1021/ar3001348.
4 Y. V. Mikhaylik and J. R. Akridge, *J. Electrochem. Soc.*, 2004, **151**, A1969–A1976, DOI: 10.1149/1.1806394.
5 M. U. M. Patel, N. D. Luong, J. Seppälä, E. Tchernychova and R. Dominko, *J. Power Sources*, 2014, **254**, 55–61, DOI: 10.1016/j.jpowsour.2013.12.081.
6 D. O-Okene, L. S. Shankar, A. Vizintin and R. Kun, *RSC Adv.*, 2025, **15**, 5381–5404, DOI: 10.1039/D4RA06245K.
7 L. Zhou, D. L. Danilov, R.-A. Eichel and P. H. L. Notten, *Adv. Energy Mater.*, 2021, **11**, 2001304, DOI: 10.1002/aenm.202001304.
8 H. Ye, J. Sun, S. Zhang, H. Lin, T. Zhang, Q. Yao and J. Y. Lee, *ACS Nano*, 2019, **13**, 14208–14216, DOI: 10.1021/acsnano.9b07121.
9 Y. Chen, Y. Liao, Y. Qing, Y. Ding, Y. Wu, L. Li, S. Luo and Y. Wu, *J. Energy Storage*, 2024, **99**, 113186, DOI: 10.1016/j.est.2024.113186.
10 W. Jan, A. D. Khan, F. J. Iftikhar, M. Z. Abbasi, G. Ali, E. Iwuoha, S. Shahzad, F. Ahmad and N. Ahmad, *Renewable Sustainable Energy Rev.*, 2025, **221**, 115916, DOI: 10.1016/j.rser.2025.115916.
11 S. Kim, J. Heo, H. Gu, H. Oh, T. Lee, Y. Lee, K. Kisu, S. Orimo, J.-W. Park and S. Kim, *Commun. Mater.*, 2025, **6**, 218, DOI: 10.1038/s43246-025-00932-x.
12 H. Hao, T. Hutter, B. L. Boyce, J. Watt, P. Liu and D. Mitlin, *Chem. Rev.*, 2022, **122**, 8053–8125, DOI: 10.1021/acs.chemrev.1c00838.
13 F. Liu, Z. Hu, J. Xue, H. Huo, J. Zhou and L. Li, *RSC Adv.*, 2019, **9**, 40471–40477, DOI: 10.1039/C9RA08238G.
14 S. Yao, H. Yu, M. Bi, C. Zhang, T. Zhang, X. Zhang, H. Liu, X. Shen and J. Xiang, *Int. J. Energy Res.*, 2022, **46**, 19585–19598, DOI: 10.1002/er.8532.
15 J. Liu, Q. Zhang and Y.-K. Sun, *J. Power Sources*, 2018, **396**, 19–32, DOI: 10.1016/j.jpowsour.2018.05.096.
16 Z. Chen, M. Lu, Y. Qian, Y. Yang, J. Liu, Z. Lin, D. Yang, J. Lu and X. Qiu, *Adv. Energy Mater.*, 2023, **13**, 2300092, DOI: 10.1002/aenm.202300092.
17 S. A. Lateef, J. Chmiola, F. Albano, W. E. Mustain and G. Jalilvand, *EES Batteries*, 2025, **1**, 947–963, DOI: 10.1039/D5EB00062A.
18 Y. Hwa and E. J. Cairns, *Electrochim. Acta*, 2018, **271**, 103–109, DOI: 10.1016/j.electacta.2018.03.040.
19 A. Vizintin, R. Guterman, J. Schmidt, M. Antonietti and R. Dominko, *Chem. Mater.*, 2018, **30**, 5444–5450, DOI: 10.1021/acs.chemmater.8b02357.
20 Y. Huang, M. Shaibani, T. D. Gamot, M. Wang, P. Jovanović, M. C. D. Cooray, M. S. Mirshekarloo, R. J. Mulder, N. V. Medhekar, M. R. Hill and M. Majumder, *Nat. Commun.*, 2021, **12**, 5375, DOI: 10.1038/s41467-021-25612-5.
21 T. Kazda, D. Capková, K. Jaššo, A. F. Straková A, E. Shembel, A. Markevich and M. Sedlaříková, *Materials*, 2021, **14**, 5578, DOI: 10.3390/ma14195578.
22 J. Liao, Z. Liu, J. Wang and Z. Ye, *ACS Omega*, 2020, **14**, 8272–8282, DOI: 10.1021/acsomega.0c00666.
23 N. P. W. Pieczonka, V. Borgel, B. Ziv, N. Leifer, V. Dargel, D. Aurbach, J.-H. Kim, Z. Liu, X. Huang, S. A. Krachkovskiy, G. R. Goward, I. Halalay, B. R. Powell and A. Manthiram, *Adv. Energy Mater.*, 2015, **5**, 1501008, DOI: 10.1002/aenm.201501008.
24 A. Raulo and G. Jalilvand, *Nano Energy*, 2024, **122**, 109265, DOI: 10.1016/j.nanoen.2024.109265.
25 O. Gröger, H. A. Gasteiger and J.-P. Suchsland, *J. Electrochem. Soc.*, 2015, **162**, A2605–A2613, DOI: 10.1149/2.0211514jes.
26 D. Yu, Q. Zhang, J. Liu, Z. Guo and L. Wangad, *J. Mater. Chem. A*, 2021, **9**, 22684–22690, DOI: 10.1039/D1TA04491E.
27 F. Liu, Z. Hu, J. Xue, H. Huo, J. Zhou and L. Li, *RSC Adv.*, 2019, **9**, 40471–40477, DOI: 10.1039/C9RA08238G.
28 Z. Zhang, W. Bao, H. Lu, M. Jia, K. Xie, Y. Lai and J. Li, *ECS Electrochem. Lett.*, 2012, **1**, A34–A37, DOI: 10.1149/2.009202eel.
29 Y. Gorlin, A. Siebel, M. Piana, T. Huthwelker, H. Jha, G. Monsch, F. Kraus, H. A. Gasteiger and M. Tromp, *J. Electrochem. Soc.*, 2015, **162**, A1146, DOI: 10.1149/2.0081507jes.
30 Q. He, A. T. S. Freiberg, M. U. M. Patel, S. Qian and H. A. Gasteiger, *J. Electrochem. Soc.*, 2020, **167**, 080508, DOI: 10.1149/1945-7111/ab8645.
31 W. Xiao, K. Yoo, J.-H. Kim and H. Xu, *Adv. Sci.*, 2023, **10**, 2303916, DOI: 10.1002/advs.202303916.
32 Y. Hwa and E. J. Cairns, *ChemElectroChem*, 2020, **7**, 3927–3934, DOI: 10.1002/celc.202000758.
33 C. J. Choi, T. H. Kim, H. W. Kim, D. M. Jeon and J. Han, *Nanomaterials*, 2025, **15**, 156, DOI: 10.3390/nano15030156.
34 H. Fazal, D. Eroglu, A. Kilic, N. Ali, C. Yan, J. Zai and X. Qian, *ChemElectroChem*, 2024, **11**, e202300781, DOI: 10.1002/celc.202300781.
35 S. Lorger, K. Narita, R. Usiskin and J. Maier, *Chem. Commun.*, 2021, **57**, 6503–6506, DOI: 10.1039/D1CC00557J.
36 H. Kim, J.-M. Kim, H.-N. Choi, K.-J. Min, S. Kansara, J.-Y. Hwang, J. H. Kim, H.-G. Jung and Y.-K. Sun, *Carbon Energy*, 2024, **6**, e578, DOI: 10.1002/cey2.578.
37 S. Walus, G. Offer, I. Hunt, Y. Patel, T. Stockley, J. Williams and R. Purkayastha, *Energy Storage Mater.*, 2018, **10**, 233–245, DOI: 10.1016/j.ensm.2017.05.017.
38 M. Gaberšček, *Nat. Commun.*, 2021, **12**, 6513, DOI: 10.1038/s41467-021-26894-5.

39 T. Momma, T. Yokoshima, H. Nara, Y. Gima and T. Osaka, *Electrochim. Acta*, 2014, **131**, 195–201, DOI: 10.1016/j.electacta.2014.01.091.
40 J. Moškon and M. Gaberšček, *J. Power Sources Adv.*, 2021, **7**, 100047, DOI: 10.1016/j.powera.2021.100047.
41 D. W. Abarbanel, K. J. Nelson and J. R. Dahn, *J. Electrochem. Soc.*, 2016, **163**, A522–A529, DOI: 10.1149/2.0901603jes.
42 N. Ogihara, Y. Itou, T. Sasaki and Y. Takeuchi, *J. Phys. Chem. C*, 2015, **119**, 4612–4619, DOI: 10.1021/jp512564f.
43 T. Q. Nguyen and C. Breitkopf, *J. Electrochem. Soc.*, 2018, **165**, E826–E831, DOI: 10.1149/2.1151814jes.
44 A. Lasia, *Electrochemical impedance spectroscopy and its applications*, Springer, 2014, https://link.springer.com/book/10.1007/978-1-4614-8933-7.
45 J. Landesfeind, J. Hattendorff, A. Ehrl, W. A. Wall and H. A. Gasteiger, *J. Electrochem. Soc.*, 2016, **163**, A1373–A1387, DOI: 10.1149/MA2017-02/4/268.
46 J. Landesfeind, D. Pritzl and H. A. Gasteiger, *J. Electrochem. Soc.*, 2017, **164**, A1773–A1783, DOI: 10.1149/2.0131709jes.
47 M. Gaberscek, J. Moskon, B. Erjavec, R. Dominko and J. Jamnik, *Electrochem. Solid-State Lett.*, 2008, **11**, A170–A174, DOI: 10.1149/2.0131709jes..
48 Z. Deng, Z. Zhang, Y. Lai, J. Liu, J. Li and Y. Liu, *J. Electrochem. Soc.*, 2013, **160**, A553–A558, DOI: 10.1149/2.026304jes.
49 J. H. Park, S. H. Kim and K. H. Ahn, *Colloids Surf., A*, 2023, **664**, 131130, DOI: 10.1016/j.colsurfa.2023.131130.
50 K. Kitamura, M. Tanaka and T. Mori, *J. Colloid Interface Sci.*, 2022, **625**, 136–144, DOI: 10.1016/j.jcis.2022.06.006.
51 S. Ohno and W. G. Zeier, *Acc. Mater. Res.*, 2021, **2**, 869–880, DOI: 10.1021/accountsmr.1c00116.
52 X. Judez, M. M-Ibañez, A. Santiago, M. Armand, H. Zhang and C. Li, *J. Power Sources*, 2019, **438**, 226985, DOI: 10.1016/j.jpowsour.2019.226985.